UDC 539.4

Electro-Thermo-Mechanical Response of Thick-Walled Piezoelectric Cylinder Reinforced by Boron-Nitride Nanotubes

A. Ghorbanpour Arani,[a,1] A. Haghshenas,[b] S. Amir,[a] M. R. Mozdianfard,[a] and M. Latifi[a]

[a] University of Kashan, Kashan, Iran

[b] Islamic Azad University, Khomaynishahr, Iran

[1] aghorban@kashanu.ac.ir; a_ghorbanpour@yahoo.com

УДС 539. 4

Электротермомеханические характеристики толстостенного пьезоэлектрического цилиндра, упрочненного нанотрубками из нитрида бора

А. Горбанпур Арани[а], А. Хагшенас[б], С. Амир[а], М. Р. Моздианфард[а], М. Летифи[а]

[а] Университет г. Кашан, Иран

[б] Исламский университет Азад Хомейнишехр, Хомейнишехр, Иран

Выполнен расчет электротермоупругих напряжений в пьезоэлектрическом полимерном толстостенном цилиндре, упрочненном нанотрубками из нитрида бора и подвергнутом электротермомеханическому нагружению. Электротермоупругие характеристики пьезоэлектрического композита, упрочненного нановолокнами, рассчитывали с помощью модифицированной микромеханической модели, позволяющей учитывать взаимосвязь между электрическими, тепловыми и упругими силовыми полями. Исходя из предположения о линейности, однородности и ортотропности материала пьезоэлектрического композита, упрочненного нановолокнами, при воздействии равномерного поля напряжений получены основные уравнения для осесимметричной деформации толстостенного цилиндра, подвергнутого равномерному внутреннему и внешнему давлению, осевой электрической нагрузке, и определена разность температур на внутреннем и внешнем радиусах цилиндра. Для условий закрепления торцов цилиндра, позволяющих изменять его длину, рассчитаны перемещения, деформации и напряжения в местах, значительно удаленных от торцов. Анализ расчетных напряжений показывает, что увеличение количества нанотрубок из нитрида бора в продольном направлении цилиндра приводит к уменьшению эффективного напряжения. В то же время анализ перемещений в радиальном направлении свидетельствует о том, что оптимальный состав композита обеспечивает 5%-ное содержание нанотрубок из нитрида бора. При нормальных условиях работы пьезоцилиндра влияние тепловых и механических факторов на величину эффективного напряжения существенно выше, чем электрических, в связи с чем данная структура пьезоэлектрического композита, упрочненного нановолокнами, больше применима для пьезодатчиков, чем для пьезоприводов.

Ключевые слова: нанотрубки из нитрида бора, пьезоэлектрический цилиндр, электротермомеханическое нагружение, расчет напряжений, микромеханическая модель.

Introduction. Electro-elastic materials are known to exhibit electromechanical coupling characteristics. They experience mechanical deformations when placed in an electric field, and become electrically polarized under mechanical loads [1]. Lately, smart composites, including piezoelectric composites under electro-thermo-mechanical fields, have been studied for extensive applications in power generation, sensors, actuators, ultrasonic transducer, aircraft and space platforms, automobile industries, offshore and submarine structures, chemical vessels and civil engineering structures [2–6]. These structures can be simplified to an orthotropic hollow cylinder, and exposed to a variety of temperature fields in various environments. Understanding mechanical behavior of these composites is prerequisite in allocating their appropriate applications. Recently, nano sized tubes such as carbon nanotubes (CNTs) and boron-nitride nanotubes (BNNTs) have been used as reinforcement in composite structures with the latter having higher thermal conductivity, better oxidation resistance at higher temperatures, and superior mechanical properties [7].

In 1969, Kawai [8] discovered a significant piezoelectric effect in polyvinyl-idene fluoride (PVDF) and considering its excellent mechanical properties while subjected to temperature continuously, PVDF has since been extensively studied [9, 10].

Bent and Hagood [11] suggested first the use of piezoelectric composite actuators for structural applications. Concept and model of a piezoelectric structural fiber for multifunctional composites was investigated by Lin and Sodano [12]. A semi-analytical method for analyzing prismatic non-homogeneous piezoelectric cylinders with arbitrary cross-sectional geometry was presented by Liu and Taciroglu [13]. Using a general stress analysis, Sayman [14] developed a model for thick or thin multi-layered composite cylinders under hydrothermal loadings and solved it for plane-strain, open and closed ends cases. Wang and Zhong [15] derived an exact solution for a two-dimensional problem of an infinitely long circular tube or bar of cylindrically anisotropic magneto-electro-elastic material under pressure load and applied the Stroh formalism for a cylindrical coordinate system. In another work, [16] investigated a finitely long laminated orthotropic circular cylindrical shell under pressure load and a uniform temperature change and applied power series together with Fourier series expansion methods. A three-phase cylindrical model was also used by Tong et al. [17] to analyze a fiber composite subjected to in-plane mechanical loads under the coupling effects of thermo, electric, magnetic and elastic fields. Frankland et al. [18] studied stress–strain curves of a polyethylene–single walled CNT (SWCNT) composite prepared by molecular dynamic simulations. Ding et al. [19] proposed an analytical method to solve the axisymmetric plane strain piezo-thermo-elastic dynamic problems of a special non-homogeneous pyroelectric hollow cylinder subjected to arbitrary axisymmetric thermal loads. Dai and Wang [20] presented an exact solution for electro-thermo-elastic transient response in piezoelectric hollow structures subjected to arbitrary thermal, radial and electric shock loads.

In this work, the stress analysis of a piezoelectric polymeric thick-walled cylinder (e.g., PVDF) reinforced by another piezoelectric material such as BNNTs and subjected to electro-thermo-elastic loading is studied. Overall properties of the piezoelectric fiber reinforced composite (PEFRC) material are evaluated as suggested by Tan and Tong [21] using an XY micromechanical model. Employing

equilibrium equations in the cylindrical coordinate for a thick-walled cylinder, and overall properties applied in the stress–strain–temperature–electric field relation, a differential equation for radial displacement is derived, which is then solved in exact form for the specified boundary conditions. Replacing the obtained radial displacement in the stress–strain relation yields radial, longitudinal and circumferential stresses, which are plotted for various boundary conditions, against temperature difference, potential difference and cylinder radius.

1. **Micromechanical Model**. As mentioned above the overall properties of the PEFRC is evaluated by a micromechanical XY model. A representative volume element (RVE) with square cross-sectional is selected for a PEFRC and a circular one for the fiber is assumed (see Fig. 1). The influence of the piezoelectric fiber volume fraction on the effective constants for PEFRC materials using the above mentioned model was investigated and the results complied well with those found with Mori–Tanaka mean field approach. The assumptions made for the XY model include:

(i) the composite material is perfectly bonded, its constituents are assumed to be linear homogeneous and orthotropic;

(ii) the applied electric and thermal fields to the PEFRC unit cell are uniform;

(iii) iso-stress and iso-electric displacement are assumed to exist across the planes which are in series with respect to the loading direction. Iso-strain and iso-electric field are assumed across the planes which are in parallel with respect to the loading direction [6];

(iv) thermal field within a PEFRC unit cell is uniform.

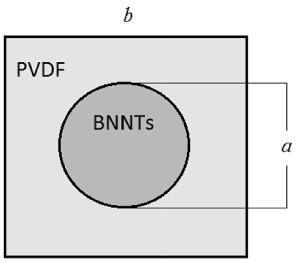

Fig. 1. Schematics of representative volume element of PEFRC.

The closed-form formulas for the effective electro-thermo-elastic constants of an X PEFRC strip may be expressed as Eqs. (1)–(11) described below:

$$C_{11}^{p} = \frac{C_{11}^{mm} C_{11}^{pp}}{\rho C_{11}^{mm} + (1-\rho) C_{11}^{pp}}, \tag{1}$$

$$C_{22}^{p} = \rho C_{22}^{pp} + (1-\rho) C_{22}^{mm} + \frac{(C_{12}^{p})^2}{(C_{11}^{p})} - \rho \frac{(C_{12}^{pp})^2}{C_{11}^{pp}} - \frac{(1-\rho)(C_{12}^{mm})^2}{C_{11}^{mm}}, \tag{2}$$

$$C_{23}^{p} = \rho C_{23}^{pp} + (1-\rho) C_{23}^{mm} + \frac{C_{12}^{pp} C_{13}^{p}}{C_{11}^{p}} - \rho \frac{C_{12}^{pp} C_{13}^{pp}}{C_{11}^{pp}} - \frac{(1-\rho) C_{12}^{mm} C_{13}^{mm}}{C_{11}^{mm}}, \tag{3}$$

$$C_{13}^{p} = C_{11}^{p}\left[\frac{\rho C_{13}^{pp}}{C_{11}^{pp}} - \frac{(1-\rho)C_{13}^{mm}}{C_{11}^{mm}}\right], \tag{4}$$

$$C_{33}^{p} = \rho C_{33}^{pp} + (1-\rho)C_{33}^{mm} + \frac{(C_{13}^{p})^2}{C_{12}^{p}} - \rho\frac{(C_{3}^{pp})^2}{C_{11}^{pp}} - \frac{(1-\rho)(C_{13}^{mm})^2}{C_{11}^{mm}}, \tag{5}$$

$$e_{31}^{p} = C_{11}^{p}\left[\frac{\rho e_{13}^{pp}}{C_{11}^{pp}} - \frac{(1-\rho)e_{13}^{mm}}{C_{11}^{mm}}\right], \tag{6}$$

$$e_{32}^{p} = \rho e_{23}^{pp} + (1-\rho)e_{23}^{mm} + \frac{C_{12}^{p}e_{13}^{p}}{C_{11}^{p}} - \rho\frac{C_{12}^{pp}e_{13}^{pp}}{C_{11}^{pp}} - \frac{(1-\rho)C_{12}^{mm}e_{13}^{mm}}{C_{11}^{mm}}, \tag{7}$$

$$e_{33}^{p} = \rho e_{33}^{pp} + (1-\rho)e_{33}^{mm} + \frac{C_{13}^{p}e_{13}^{p}}{C_{11}^{p}} - \rho\frac{C_{13}^{pp}e_{13}^{pp}}{C_{11}^{pp}} - \frac{(1-\rho)C_{13}^{mm}e_{13}^{mm}}{C_{11}^{mm}}, \tag{8}$$

$$\lambda_{1}^{p} = C_{11}^{p}\left[\frac{\rho\lambda_{1}^{pp}}{C_{11}^{pp}} - \frac{(1-\rho)\lambda_{11}^{mm}}{C_{11}^{mm}}\right], \tag{9}$$

$$\lambda_{3}^{p} = \rho\lambda_{3}^{pp} + (1-\rho)\lambda_{3}^{mm} + \frac{C_{13}^{p}\lambda_{1}^{p}}{C_{11}^{p}} - \rho\frac{C_{13}^{pp}\lambda_{2}^{p}}{C_{11}^{pp}} - \frac{(1-\rho)C_{13}^{mm}\lambda_{1}^{mm}}{C_{11}^{mm}}, \tag{10}$$

$$\lambda_{2}^{p} = \rho\lambda_{22}^{pp} + (1-\rho)\lambda_{22}^{mm} + \frac{C_{12}^{p}\lambda_{1}^{p}}{C_{11}^{p}} - \rho\frac{C_{12}^{pp}\lambda_{2}^{p}}{C_{11}^{pp}} - \frac{(1-\rho)C_{12}^{mm}\lambda_{1}^{mm}}{C_{11}^{mm}}, \tag{11}$$

where C_{ij}, e_{mn}, and λ_{p} are elastic stiffness constants, piezoelectric constants, and thermal expansion, respectively. The constant $\rho = \frac{x_a}{x_b} - \frac{y_a}{y_b}$ (where x_a, x_b and y_a, y_b are dimensions of fiber and matrix unit cells, respectively) as illustrated in Fig. 1. For the Y PEFRC model, the corresponding equations can be obtained by simply exchanging the subscripts 1 with 2 in the above Eqs. (1)–(10). Hence, the effective constants of XY model was obtained by placing the effective constitutive coefficients of X model into the effective fiber coefficients of Y model. The resulting formulations are presented in Eqs. (12)–(23) below which represent the mechanical properties for the defined RVE:

$$C_{11} = \rho C_{11}^{p} + (1-\rho)C_{11}^{m} + \frac{C_{12}^{2}}{C_{22}} - \rho\frac{(C_{12}^{p})^2}{C_{22}^{p}} - \frac{(1-\rho)(C_{12}^{m})^2}{C_{22}^{m}}, \tag{12}$$

$$C_{12} = C_{22}\left[\frac{\rho C_{12}^{p}}{C_{22}^{p}} - \frac{(1-\rho)C_{12}^{m}}{C_{22}^{m}}\right], \tag{13}$$

$$C_{13} = \rho C_{13}^{p} + (1-\rho)C_{13}^{m} + \frac{C_{12}C_{23}}{C_{22}} - \rho\frac{C_{12}^{p}C_{23}^{p}}{C_{22}^{p}} - \frac{(1-\rho)C_{12}^{m}C_{23}^{m}}{C_{22}^{m}}, \tag{14}$$

$$C_{22} = \frac{C_{22}^{p}C_{22}^{m}}{\rho C_{22}^{m} + (1-\rho)C_{22}^{p}}, \tag{15}$$

$$C_{23} = C_{22}\left[\frac{\rho C_{23}^{2}}{C_{22}^{p}} - \frac{(1-\rho)C_{23}^{m}}{C_{22}^{m}}\right], \tag{16}$$

$$C_{33} = \rho C_{33}^{p} + (1-\rho)C_{33}^{m} + \frac{C_{23}^{3}}{C_{22}} - \rho\frac{(C_{23}^{p})^{2}}{C_{22}^{p}} - \frac{(1-\rho)(C_{23}^{m})^{2}}{C_{22}^{m}}, \tag{17}$$

$$e_{31} = \rho e_{31}^{p} + (1-\rho)e_{31}^{m} + \frac{C_{12}e_{32}}{C_{22}} - \rho\frac{C_{12}^{p}e_{32}^{p}}{C_{22}^{p}} - \frac{(1-\rho)C_{12}^{m}e_{32}^{m}}{C_{22}^{m}}, \tag{18}$$

$$e_{32} = C_{22}\left[\frac{\rho e_{32}^{2}}{C_{22}^{p}} - \frac{(1-\rho)e_{32}^{m}}{C_{22}^{m}}\right], \tag{19}$$

$$e_{33} = \rho e_{33}^{p} + (1-\rho)e_{33}^{m} + \frac{C_{23}e_{32}}{C_{22}} - \rho\frac{C_{23}^{p}e_{32}^{p}}{C_{22}^{p}} - \frac{(1-\rho)C_{23}^{m}e_{32}^{m}}{C_{22}^{m}}, \tag{20}$$

$$\lambda_1 = \rho\lambda_1^{p} + (1-\rho)\lambda_1^{m} + \frac{C_{12}\lambda_2}{C_{22}} - \rho\frac{C_{12}^{p}\lambda_2^{p}}{C_{22}^{p}} - \frac{(1-\rho)C_{12}^{m}\lambda_2^{m}}{C_{22}^{m}}, \tag{21}$$

$$\lambda_3 = \rho\lambda_3^{p} + (1-\rho)\lambda_3^{m} + \frac{C_{23}\lambda_2}{C_{22}} - \rho\frac{C_{23}^{p}\lambda_2^{p}}{C_{22}^{p}} - \frac{(1-\rho)C_{23}^{m}\lambda_2^{m}}{C_{22}^{m}}, \tag{22}$$

$$\lambda_2 = C_{22}\left[\frac{\rho\lambda_2^{p}}{C_{22}^{p}} - \frac{(1-\rho)\lambda_2^{m}}{C_{22}^{m}}\right]. \tag{23}$$

2. **Fundamental Relations**. Figure 2 demonstrates a thick-walled cylinder, subjected to uniform internal and external pressures (P_i and P_o, respectively), and a radial temperature change ΔT, in an axial electrical field. The temperature change ΔT is a function of the radial coordinate r only and hence, cylinder

deformation is axially symmetric. Furthermore, the deformations happen at a cross section sufficiently far removed from the junction of the cylinder and its end caps, so that it is practically independent of the axial coordinate z as suggested by Boresi et al. [22].

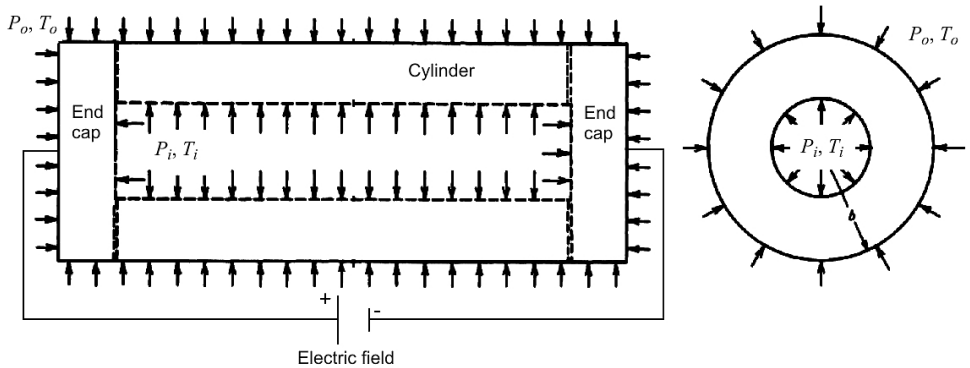

Fig. 2. A closed cylinder with internal pressure, external pressure, radial temperature, and axial electric fields.

2.1. ***Heat Conduction Analysis***. Steady-state temperature distribution in a homogeneous body in the absence of any heat source may be presented by the Fourier heat equation as

$$\nabla^2 T = 0. \tag{24}$$

For symmetric thermal conduction, the heat equation in a cylindrical coordinate (r, θ, z) can be written as

$$\frac{\partial^2 T}{\partial r^2} + \frac{1}{r}\frac{\partial T}{\partial r} = 0, \tag{25}$$

which could be solved in the following form

$$T_r = k_1 + k_2 \ln(r), \tag{26}$$

where k_1 and k_2 are integration constants. The boundary conditions $T = T_i$ when $r = r_i$, and $T = T_o$ when $r = r_o$ allows k_1 and k_2 to be determined as

$$k_2 = \frac{(T_i - T_o)}{\ln(r_i) - \ln(r_o)}, \qquad k_1 = T_i - k_2 \ln(r_i). \tag{27}$$

2.2. ***Governing Equations***. In thick-walled cylinder with end caps there are only three stress components of σ_r, σ_θ, and σ_z (radial, circumferential, and axial stresses, respectively) all of which are function of radius. Ignoring body force component, the equilibrium equation in radial direction becomes [22]

$$\frac{\partial \sigma_r}{\partial_r} + \frac{\sigma_r - \sigma_\theta}{r} = 0. \tag{28}$$

The electrical equilibrium equation is know from [1] as

$$\frac{1}{r}(rD_r)_{,r} + \frac{1}{r}D_{\theta,\theta} + D_{z,z} = 0, \tag{29}$$

where D_r, D_θ, and D_z are component of radial, circumferential, and longitudinal electric displacement, respectively.

The composite material of the cylinder is assumed to be orthotropic and linearly elastic. Therefore, the stress–strain–temperature–electric field relations may be given as [1]

$$\begin{bmatrix}\sigma_r\\ \sigma_\theta\\ \sigma_z\end{bmatrix} = \begin{bmatrix}C_{11} & C_{12} & C_{13}\\ C_{12} & C_{22} & C_{23}\\ C_{31} & C_{32} & C_{33}\end{bmatrix}\begin{bmatrix}\varepsilon_r\\ \varepsilon_\theta\\ \varepsilon_z\end{bmatrix} - \begin{bmatrix}0 & 0 & e_{13}\\ 0 & 0 & e_{23}\\ 0 & 0 & e_{33}\end{bmatrix}\begin{bmatrix}E_r\\ E_\theta\\ E_z\end{bmatrix} - \begin{bmatrix}\lambda_r\\ \lambda_\theta\\ \lambda_z\end{bmatrix}\Delta T \tag{30}$$

and

$$\begin{bmatrix}D_r\\ D_\theta\\ D_z\end{bmatrix} = \begin{bmatrix}0 & 0 & 0\\ 0 & 0 & 0\\ e_{31} & e_{32} & e_{33}\end{bmatrix}\begin{bmatrix}\varepsilon_r\\ \varepsilon_\theta\\ \varepsilon_z\end{bmatrix} + \begin{bmatrix}\in_{11} & 0 & 0\\ 0 & \in_{22} & 0\\ 0 & 0 & \in_{33}\end{bmatrix}\begin{bmatrix}E_r\\ E_\theta\\ E_z\end{bmatrix}, \tag{31}$$

where λ_r, λ_θ, and λ_z may also be expressed as

$$\begin{aligned}\lambda_r &= C_{11}\alpha_r + C_{12}\alpha_\theta + C_{13}\alpha_z,\\ \lambda_\theta &= C_{21}\alpha_r + C_{22}\alpha_\theta + C_{23}\alpha_z,\\ \lambda_z &= C_{31}\alpha_r + C_{32}\alpha_\theta + C_{33}\alpha_z,\end{aligned} \tag{32}$$

where ε and α correspond to strain and thermal expansion, respectively, and subscript r, θ, and z denote respectively the radial, circumferential, and longitudinal components. The strain–displacement relations are therefore

$$\begin{aligned}\varepsilon_r &= \frac{\partial u_r}{\partial r},\\ \varepsilon_\theta &= \frac{u_r}{r},\\ \varepsilon_z &= \frac{\partial u_z}{\partial z},\end{aligned} \tag{33}$$

where $u_r = u_r(r, z)$ and $u_z = u_z(r, z)$ represents displacement components in the r and z direction, respectively [21]. It should be noted that $\in_{33}$ and E_z represent dielectric constant and electric field in longitudinal direction, respectively, and

$$E_z = -\frac{\partial \phi}{\partial z}. \tag{34}$$

Since u_r and u_z do not depend much on z at a cross section far removed from the end, the shear strain components become zero due to radial symmetry, in which case ε_z could be assumed constant, therefore

$$\varepsilon_z = \frac{\partial u_z}{\partial z} = a. \tag{35}$$

3. **Analytical Solution**. In order to solve this problem, the exact solution is adopted. The electric field is applied in z direction. However, considering Eq. (31), D_r and D_θ are zero, therefore Eq. (29) reduces to

$$\frac{\partial D_z}{\partial z} = 0. \tag{36}$$

Considering D_z component in Eq. (31) and Eq. (35), the electrical equilibrium Eq. (36) may be written as the following differential equation

$$\in_{33} \frac{\partial^2 \phi_z}{\partial z^2} = 0, \tag{37}$$

which could be solved by multiple integration with respect to z into the following format

$$\phi_z = \alpha z + \beta, \tag{38}$$

where α and β are integral constants to be evaluated considering the two boundary conditions below on a thick-walled piezoelectric cylinder

$$\begin{aligned} \phi_z &= \phi_0 \quad \text{at} \quad z = 0, \\ \phi_z &= \phi_L \quad \text{at} \quad z = L, \end{aligned} \tag{39}$$

which yield

$$\beta = \phi_0, \qquad \alpha = \frac{\phi_L - \phi_0}{L}. \tag{40}$$

The governing differential equation for the problem can now be obtained by substituting Eqs. (30), (32), (33), (35) and (38), into Eq. (28)

$$C_{11} r^2 \frac{\partial^2 u_r}{\partial z^2} + C_{11} r \left(\frac{\partial u_r}{\partial r} \right) - C_{22}(u_r) = Pr + Qr \ln r + rak, \tag{41}$$

where Q, P, k, N, and M are constants, defined as

$$\begin{gathered} k = (C_{23} - C_{13}), \qquad M = (\lambda_r - \lambda_\theta), \qquad N = (e_{32} - e_{31}), \\ P = (N + Mk_1 + \lambda_r k_2), \qquad Q = (Mk_2). \end{gathered} \tag{42}$$

The governing equation (41) is the Cauchy–Euler non-homogeneous differential equation whose solution is

$$u_r = C_1 r^{A_1} + C_2 r^{-A_1} + A_2 r \ln r + A_3 r + A_4 a r, \tag{43}$$

where C_1 and C_2 are constants which could be obtained from boundary condition associated with internal and external pressure stresses explained below. Constants A_1, A_2, A_3, and A_4 are defined as

$$A_1 = \left(\frac{C_{22}}{C_{11}}\right)^{1/2}, \qquad A_2 = \frac{Q}{C_{11} - C_{22}}, \qquad A_3 = \frac{C_{11}(P - 2Q) - C_{22}P}{(C_{11} - C_{22})^2}, \qquad A_4 = \frac{k}{C_{11} - C_{22}}. \tag{44}$$

Substituting Eq. (43) into Eq. (33) and substituting the resulting equation into the first row of Eq. (30), yields the expression for radial stress (σ_r) as

$$\sigma_r = C_1 r^{H_1} H_2 + C_2 r^{H_3} H_4 + G_1 \ln r + G_2 + G_3 a, \tag{45}$$

where the following constants could be defined as

$$\begin{gathered} H_1 = A_1 - 1, \qquad H_2 = (C_{11}A_1 + C_{12}), \qquad H_3 = (-A_1 - 1), \\ H_4 = [C_{11}(-A_1) + C_{12}], \qquad G_1 = (C_{11}A_2 + C_{12}A_2 - \lambda_r k_2), \\ G_2 = (A_2 C_{11} + A_3 C_{11} + C_{12}A_3 + e_{13}\alpha - \lambda_r k_1), \\ G_3 = (A_4 C_{11} + C_{12}A_4 + C_{13}). \end{gathered} \tag{46}$$

In order to find C_1 and C_2 in Eq. (45) above, the following pressure boundary conditions on the inner and outer surfaces of the cylinder are considered

$$\begin{aligned} \sigma_r &= -P_i \quad \text{at} \quad r = r_i, \\ \sigma_r &= -P_o \quad \text{at} \quad r = r_o. \end{aligned} \tag{47}$$

Replacing these in the radial stress Eq. (45) gives

$$C_1 = J_1 + J_2 a, \qquad C_2 = J_3 + J_4 a. \tag{48}$$

where

$$J_1 = \frac{r_i^{H_3} P_o + r_i^{H_3} G_1 \ln(r_o) + r_i^{H_3} G_2 - P_i r_o^{H_3} - G_1 \ln(r_i) r_o^{H_3} - G_2 r_o^{H_3}}{H_2(-r_i^{H_3} r_0^{H_1} - r_o^{H_3} r_i^{H_1})},$$

$$J_2 = \frac{r_i^{H_3} G_3 - G_3 r_i^{H_3}}{H_2(-r_i^{H_3} r_o^{H_1} - r_o^{H_3} r_i^{H_1})},$$

$$J_3 = -\left(\frac{-r_o^{H_3} P_i + r_o^{H_1} G_1 \ln(r_i) + r_o^{H_1} G_2 - P_o r_i^{H_1} + G_1 \ln(r_o) r_i^{H_1} - G_2 r_i^{H_1}}{H_4(-r_i^{H_3} r_o^{H_1} - r_o^{H_3} r_i^{H_1})} \right),$$

$$J_4 = \frac{r_o^{H_1} G_3 - G_3 r_o^{H_1}}{H_4(-r_i^{H_3} r_o^{H_3} - r_o^{H_3} r_i^{H_1})}. \tag{49}$$

As can be seen C_1 and C_2 are defined in term of another constant a which need be determined considering another boundary condition, i.e., the equation for overall equilibrium forces along the longitudinal axial direction. This equation is obtained by balancing the axial electrical and mechanical forces involved and may be written as

$$\int_{r_i}^{r_o} \sigma_z 2\pi r dr = e_{33}(\alpha)\pi(r_o^2 - r_i^2) + \pi(P_i r_i^2 - P_o r_o^2). \tag{50}$$

It is noteworthy that the temperature change ΔT does not appear in Eq. (50). This is because the effects of temperature are self-equilibrating, i.e., the thermal loads on the cylinder surface in longitudinal direction balances out each other and the overall thermal load becomes zero. Also, the electric field is considered as an axial load here that is applied to the cylinder closed ends. Equation (50) may be one of the major contributions of this study, as it is perhaps the first time electric field is considered in this developed and solved governing equation in the form of an applied axial load for a three dimensional geometry. Other contributions of this paper include using the XY micromechanical model to evaluate the overall physical characteristics of the composite, which enabled us to compute both the overall piezoelectric and thermal constants of the composite on top of other mechanical properties associated with the problem. Assuming orthotropic matrix meant we had to choose the more complex XY model to solve the problem.

4. **Numerical Results and Discussion**. At this point, numerical results are obtained for circumferential, longitudinal and effective stresses in a thick-walled composite cylinder made from PVDF and reinforced by DWBNNTs subjected to internal and external pressures, axial electric field and radial thermal field. Table 1 presents physical characteristics of both the orthotropic PVDF matrix and DWBNNTs reinforcement fibers of the smart composite used in this study [7] and [23].

The cylinder considered for this study is assumed to have inner radius $20 \cdot 10^{-6}$ m, outer radius $23 \cdot 10^{-6}$ m, length $100 \cdot 10^{-6}$ m. Internal and external temperatures are 30 and 60°C, respectively. Applied voltage is $\phi_0 = 10$ kV. Internal and external pressures are assumed to be -100 MPa and zero, respectively. All quantities of stresses, displacements, temperatures and voltages have become dimensionless with respect to PVDF yield stress ($\sigma_Y = 54$ GPa), outer radius (r_o), internal temperature (T_i), and $\phi_L = 10$ kV, respectively, as indicated in Eq. (51) below:

$$\Sigma_r = \frac{\sigma_r}{\sigma_Y}, \quad \Sigma_\theta = \frac{\sigma_\theta}{\sigma_Y}, \quad \Sigma_z = \frac{\sigma_z}{\sigma_Y}, \quad \Sigma_e = \frac{\sigma_e}{\sigma_Y}, \quad U_r = \frac{u_r}{r_o}, \quad R = \frac{r}{r_o}. \tag{51}$$

T a b l e 1

Physical Characteristics of PVDF and DWBNNTs

Properties	BNNTs	PVDF	Properties	BNNTs	PVDF
C_{11}	2.770 TPa	10.64 GPa	e_{33}	0	−0.130
C_{12}	1.427 TPa	1.92 GPa	e_{23}	0	−0.145
C_{13}	1.427 TPa	2.19 GPa	e_{13}	0.950	−0.276
C_{22}	2.770 TPa	23.60 GPa	α_r	$0.6\cdot10^{-6}$	$7.1\cdot10^{-5}$
C_{23}	1.427 TPa	3.98 GPa	α_θ	$0.6\cdot10^{-6}$	$7.1\cdot10^{-5}$
C_{33}	2.770 TPa	238.24 GPa	α_z	$1.2\cdot10^{-6}$	$7.1\cdot10^{-5}$

Figure 3 shows the graph of dimensionless radial displacement, U_r, against cylinder radius, R, for various DWBNNT contents (ρ). Addition of DWBNNT increases cylinder stiffness considerably and reduces the radial displacement. The slope in this diagram indicates that the cylinder radial strain (ε_r), is maximum at $\rho = 0$, and almost zero for all other values of ρ. This is expected as small addition of DWBNNTs has reduced considerably ε_r. The improvement in reduction of radial displacement due to incremental addition of ρ is more significant with the smallest increase taking place at $\rho = 5\%$, leading to largest drop in radial displacement indicating that possibly 5% is the optimum DWBNNT content for the cylinder investigated here.

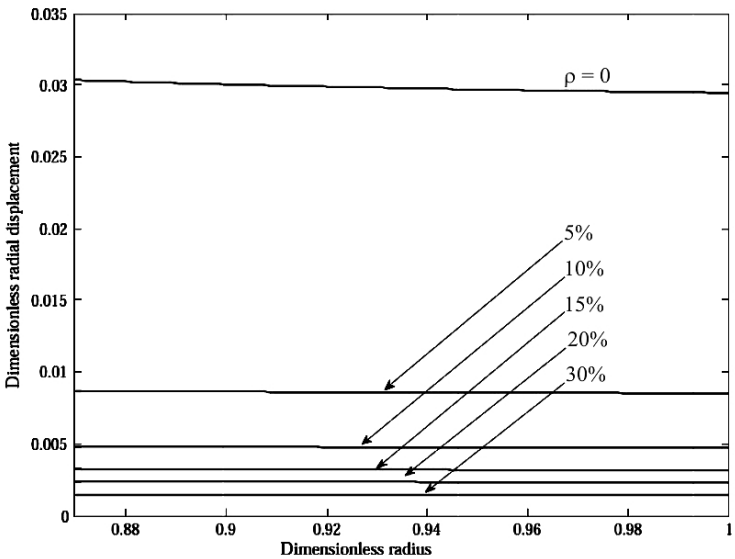

Fig. 3. Dimensionless radial displacement versus the radius of the smart composite cylinder for different content of DWBNNT.

Figures 4, 5, and 6 illustrate the dimensionless circumferential stress, axial stress, and effective stress against the cylinder radius for different values of ρ. As can be seen, the maximum circumferential stress occurs at the internal radius of the cylinder (0.87), and the maximum axial stress occurs at the external radius.

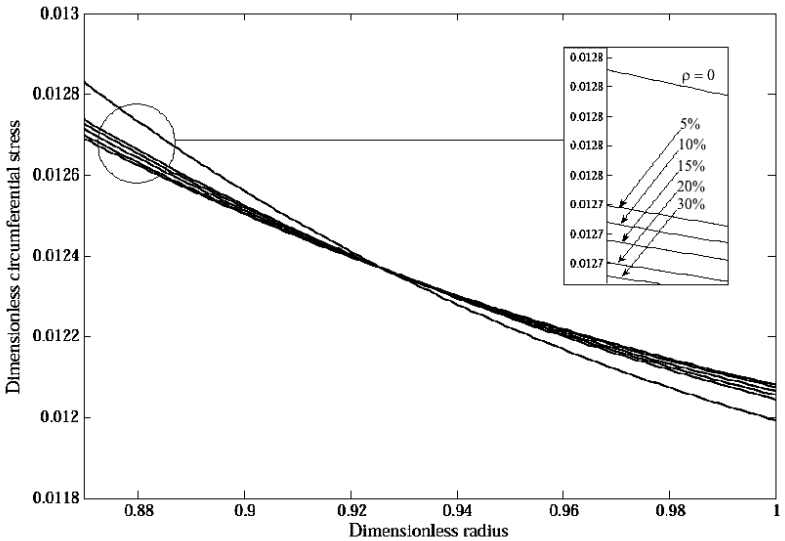

Fig. 4. Dimensionless circumferential stress versus the radius of the smart composite cylinder for different content of DWBNNT.

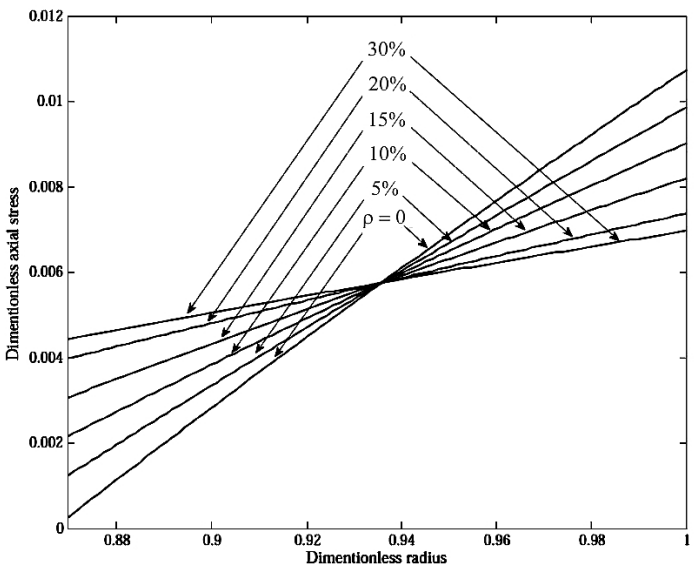

Fig. 5. Dimensionless axial stress versus the radius of the smart composite cylinder for different content of DWBNNT.

Effective stress obtained on the basis of the von Mises indicates that it is maximum at both internal and external radii of the cylinder. As ρ is increased from 0 to 30%, the maximum circumferential, axial and effective stresses are reduced to the extent that the effective stress is reduced by almost 75%. The same as Fig. 3, the significant incremental improvement in reduced circumferential stress, occurs at $\rho = 5\%$, indicating this value to be a possible optimum for crack resistance. It is also interesting to note that axial stress, σ_z, has become a function of the radius simply due to temperature difference across the internal and external radii, otherwise σ_z would have been a fixed value.

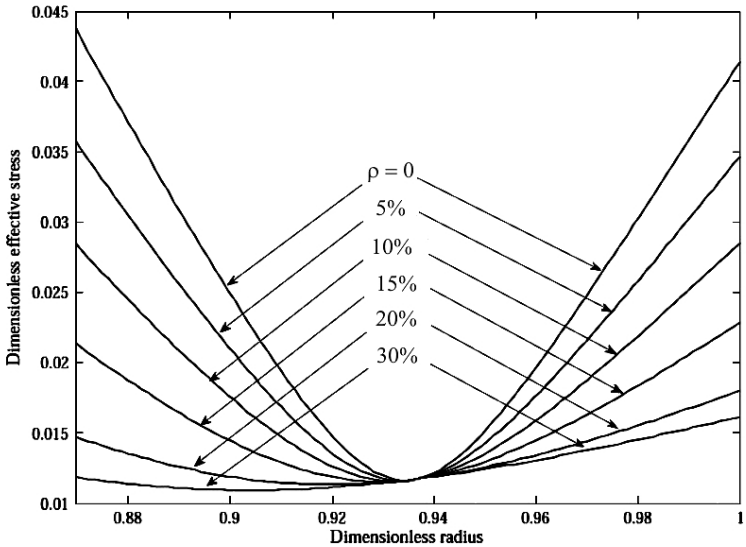

Fig. 6. Dimensionless effective stress (based on the von Mises criterion) versus the radius of the smart composite cylinder for different content of DWBNNT.

Figures 7, 8, 9, and 10 illustrate the effect of electric field on the U_r, Σ_θ, Σ_z, and Σ_e along the radius of the cylinder at $\rho = 5\%$ and voltages of -10, 0, and 10 kV. As can be seen, the effect of electric field in general is insignificant. Nevertheless, it has caused more displacement at the outer radius of the cylinder and positive/negative voltages have led to positive/negative displacements, respectively. The maximum stresses occur at the internal radius of the cylinder at negative voltage.

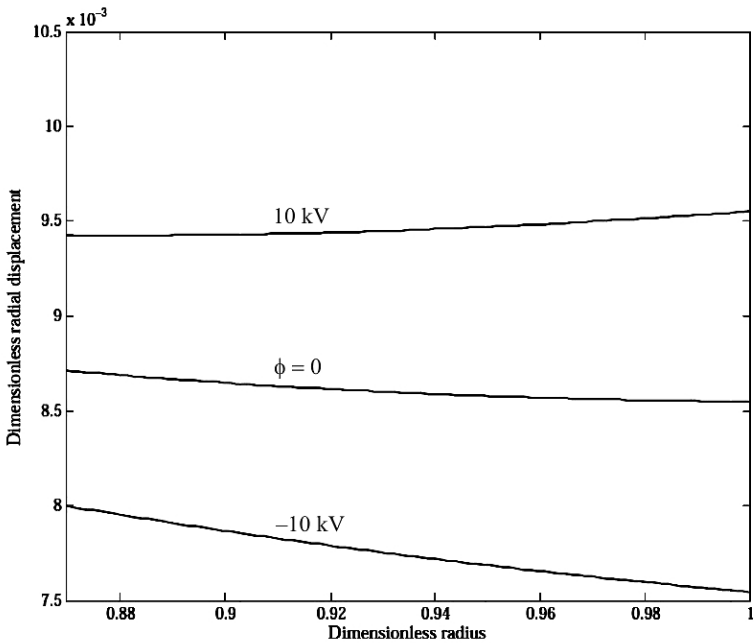

Fig. 7. Dimensionless radial displacement versus the radius of the smart composite cylinder for different voltages.

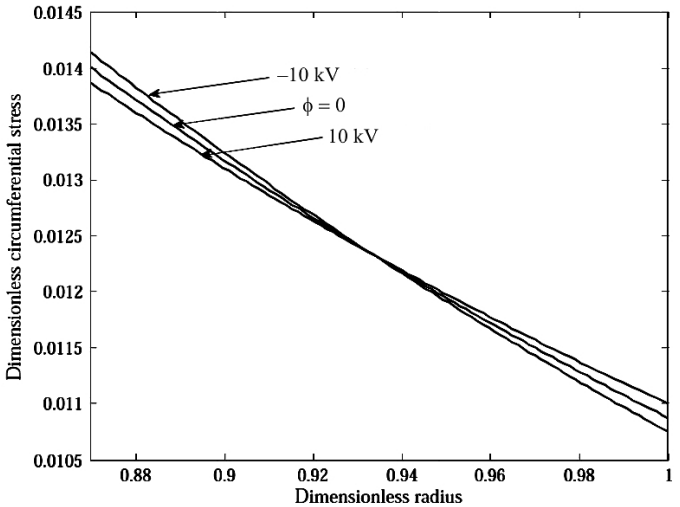

Fig. 8. Dimensionless circumferential stress versus the radius of the smart composite cylinder for different voltages.

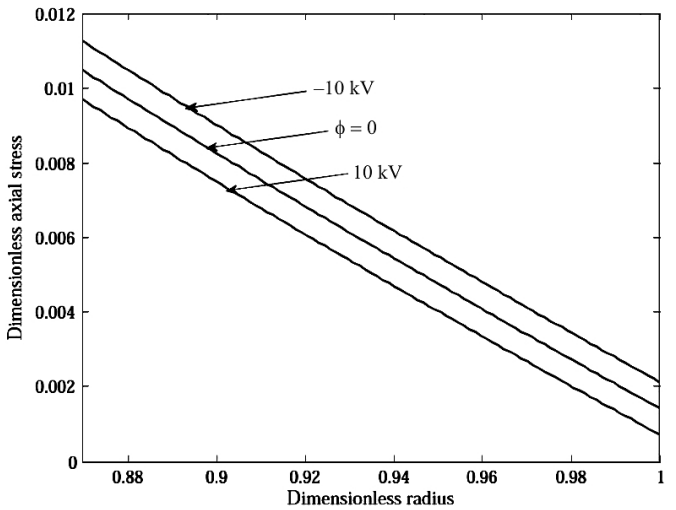

Fig. 9. Dimensionless axial stress versus the radius of the smart composite cylinder for different voltages.

Considering the importance of temperature effects on the polymeric composite, Fig. 11 demonstrates the graphs of dimensionless radial displacement, U_r, versus r for three different internal temperatures, 30, 45, and 60℃, while the external temperature remains 30℃. The maximum displacement occurs at the internal radius of the cylinder and increasing temperature causes increase in U_r.

Figures 12, 13, and 14 illustrates the variations of Σ_θ, Σ_z, and Σ_e along r for various internal temperatures of $T_i = 30$, 45, and 60℃, while the external temperature T_o is kept constant at 30℃. The maximum Σ_θ occurs at 30℃ at the internal radius of the cylinder and increase in the T_i leads to Σ_θ reduction. As can be seen in Fig. 13, in the absence of temperature gradient between the inner and outer radii of the cylinder, (i.e., $T_i = T_o = 30°\text{C}$), the Σ_z is independent of R.

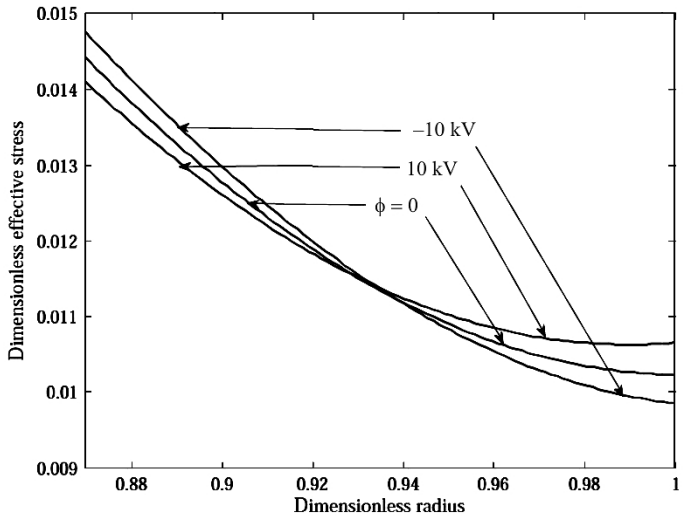

Fig. 10. Dimensionless effective stress versus the radius of the smart composite cylinder for different voltages.

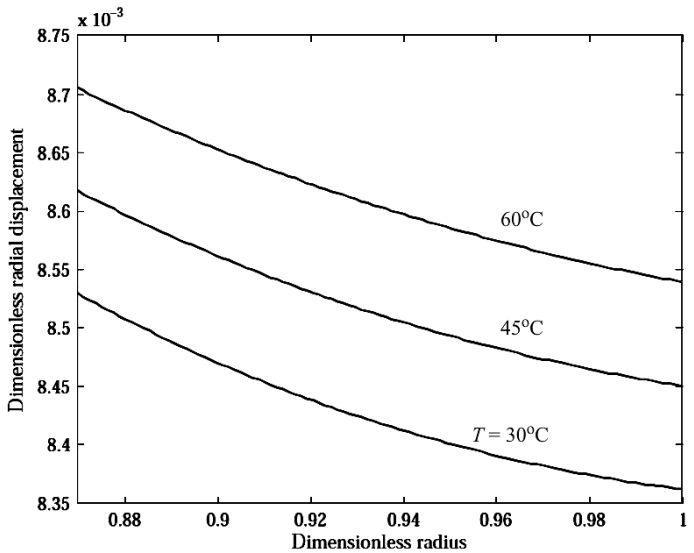

Fig. 11. Dimensionless radial displacement versus the radius of the smart composite cylinder for different internal temperatures, with external temperature at 30°C.

Increase in T_i however, reduces Σ_z to a minimum at inner radius and increases Σ_z to a maximum at outer radius of the cylinder, which is justifyable due to the self equilibrating nature of temperature field. This behavior of the Σ_z however, indicate validation of the governing equations developed including Eq. (50). The effective stress (Fig. 14) at various T_i illustrate that Σ_e is maximum in the internal radius and is highest as T_i increases at both inner and outer radii of the smart composite cylinder.

Conclusions. In this article, displacement, and circumferential, axial and effective stresses of a thick-walled smart composite cylinder with end-caps, made from piezoelectric materials (PVDF reinforced by DWBNNT's) and subjected to

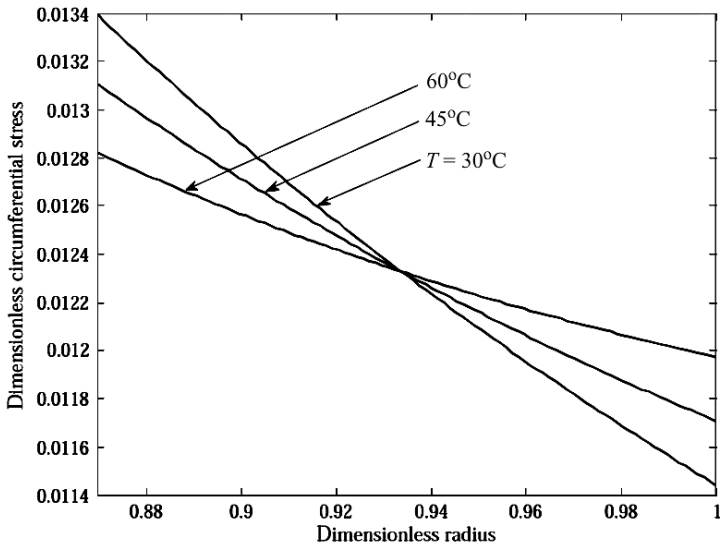

Fig. 12. Dimensionless circumferential stress versus the radius of the smart composite cylinder for different internal temperatures, with external temperature at 30°C.

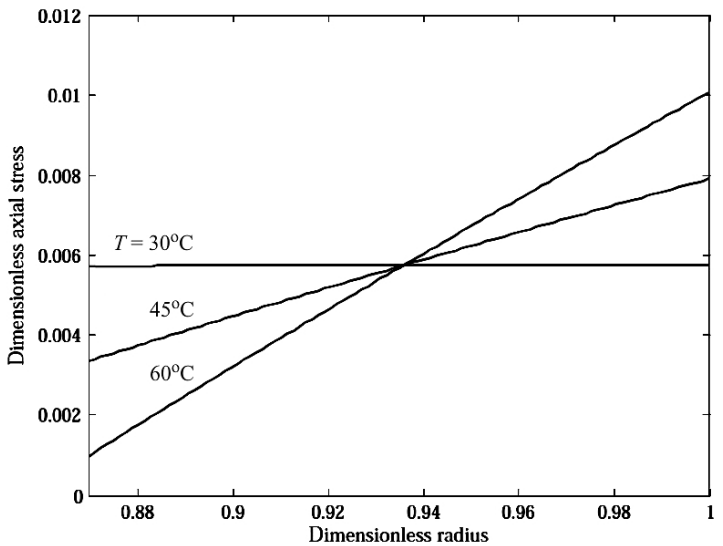

Fig. 13. Dimensionless axial stress versus the radius of the smart composite cylinder for different internal temperatures, with external temperature at 30°C.

mechanical, electrical and thermal fields are studied. Apart from the piezoelectric nature of the materials used and the associated model for evaluating the overall mechanical characteristics, the contribution of the paper include consideration of 3D structural analysis and orthotropic composite matrix. The results suggest that increasing DWBNNTs content reduces stresses associated with mechanical, thermal, and electrical fields, in descending order. Also, at normal working conditions, the influence of thermal and mechanical fields are much higher than the electric one on the effective stress; hence, this smart structure is best suited for applications as sensors than actuators.

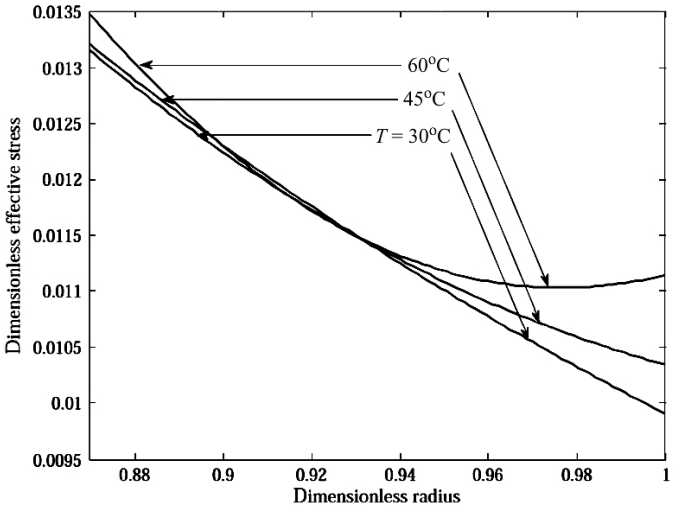

Fig. 14. Dimensionless effective stress versus the radius of the smart composite cylinder for different internal temperatures, with external temperature at 30℃.

Р е з ю м е

Виконано розрахунок електротермопружних напружень у п'єзоелектричному циліндрі, зміцненому нанотрубками з нитриду бору та підданому електротермомеханічному навантаженню. Електротермопружні характеристики п'єзоелектричного композита, зміцненого нановолокнами, розраховували за допомогою модифікованої мікромеханічної моделі, що дозволяє враховувати взаємозв'язок між електричними, тепловими і пружними силовими полями. На основі припущення про лінійність, однорідність та ортотропність матеріалу п'єзоелектричного композита, зміцненого нановолокнами, при дії рівномірного поля напружень отримано основні рівняння для осесиметричної деформації товстостінного циліндра, що знаходиться під дією рівномірного внутрішнього і зовнішнього тиску, осьового електричного навантаження, і визначено різницю температур на внутрішньому і зовнішньому радіусах циліндра. Для умов закріплення торців циліндра, що дозволяє змінити його довжину, розраховано переміщення, деформації і напруження в місцях на значній відстані від торців. Аналіз розрахункових напружень показує, що зі збільшенням нанотрубок із нітриду бору в поздовжньому напрямку циліндра зменшується ефективне напруження. У той же час аналіз переміщень у радіальному напрямку свідчить, що оптимальний склад композита забезпечує 5%-ний вміст нанотрубок із нітриду бору. За нормальних умов роботи п'єзоциліндра вплив теплових і механічних чинників на величину ефективного напруження суттєво вищий, аніж електричних, у зв'язку з чим дана структура п'єзоелектричного композита, зміцненого нановолокнами, більше використовується для п'єзодатчиків, ніж для п'єзоприводів.

1. J. Yang, *An Introduction to the Theory of Piezoelectricity*, Springer (2005).
2. E. F. Crawley, "Intelligent structures for aerospace: a technology overview and assessment," *AIAA J.*, **32**, No. 8, 1689–1699 (1994).

3. M. Arafa and A. Baz, "Dynamics of active piezoelectric damping composites," *Composites Part B*, **31**, 255–264 (2000).
4. G. Park, M. H. Kim, and D. J. Inman, "Integration of smart materials into dynamics and control of inflatable space structures," *J. Intell. Mater. Syst. Struct.*, **12**, No. 6, 423–433 (2002).
5. H. A. Sodano, J. Lloyd, and D. J. Inman, "An experimental comparison between several active composite actuators for power generation," *Smart Mater. Struct.*, **15**, 1211–1216 (2006).
6. Y. Shindo, F. Narita, and H. Sosa, "Electroelastic analysis of a piezoelectric ceramic strip with a central crack," *Int. J. Eng. Sci.*, **38**, 1–19 (1998).
7. A. Salehi-Khojin and N. Jalili, "Buckling of boron nitride nanotube reinforced piezoelectric polymeric composites subject to combined electro-thermo-mechanical loadings," *Compos. Sci. Technol*., **68**, 1489–1501 (2008).
8. H. Kawai, "The piezoelectricity of polyvinylidene fluoride," *Jpn. J. Appl. Phys.*, **8**, 975–976 (1969).
9. W. V. Munch and U. Thiemann, "Pyroelectric detector array with PVDF on silicon integrated circuit," *Sens. Actuators A*, **25-27**, 167–172 (1991).
10. H. S. Tzou and R. Ye, "Pyroelectric and thermal strain effects in piezoelectric (PVDF and PZT) devices," *Mech. Syst. Sig. Process*, **10**, No. 4, 459–479 (1996).
11. A. A. Bent and N. W. Hagood, "Piezoelectric fiber composites with interdigitated electrodes," *J. Intell. Mater. Syst. Struct.*, **8**, 903–919 (1997).
12. Y. Lin and H. A. Sodano, "Concept and model of a piezoelectric structural fiber for multifunctional composites," *Compos. Sci. Technol.*, **68**, 1911–1918 (2008).
13. C. W. Liu and E. Taciroglu, "A semi-analytic meshfree method for Almansi–Michell problems of piezoelectric cylinders," *Int. J. Solids Struct*., **45**, No. 9, 2379–2398 (2008).
14. O. Sayman, "Analysis of multi-layered composite cylinders under hygro-thermal loading," *Composites Part A*, **36**, 923–933 (2005).
15. X. Wang and Z. Zhong, "A circular tube or bar of cylindrically anisotropic magnetoelectroelastic material under pressuring loading," *Int. J. Eng. Sci*., **41**, 2143–2159 (2003).
16. X. Wang and Z. Zhong, "A finitely long circular cylindrical shell of piezo-electric/piezomagnetic composite under pressuring and temperature change," *Int. J. Eng. Sci.*, **41**, 2429–2445 (2003).
17. Z. H. Tong, S. H. Lo, C. P. Jiang, and Y. K. Cheung, "An exact solution for the three-phase thermo-electro-magneto-elastic cylinder model and its application to piezoelectric-magnetic fiber composites," *Int. J. Solids Struct*., **45**, 5205–5219 (2008).
18. S. J. V. Frankland, V. M. Harik, G. M. Odegard, et al., "The stress-strain behavior of polymer–nanotube composites from molecular dynamics simulation," *Compos. Sci. Technol*., **63**, 1655–1661 (2003).

19. H. J. Ding, H. M. Wang, and W. Q. Chen, "Analytical solution of a special non-homogeneous pyroelectric hollow cylinder for piezothermoelastic axisymmetric plane strain dynamic problems," *Appl. Math. Comput*., **151**, 423–441 (2004).
20. H. L. Dai and X. Wang, "Thermo-electro-elastic transient responses in piezoelectric hollow structures," *Int. J. Solids Struct*., **42**, No. 3, 1151–1171 (2005).
21. P. Tan and L. Tong, "Modeling for the electro-magneto-thermo-elastic properties of piezoelectric-magnetic fiber reinforced composites," *Composites Part A*, **33**, 631–645 (2002).
22. A. P. Boresi, R. J. Schmidt, and O. M. Sidebottom, *Advanced Mechanics of Materials*, 5 ed., John Wiley & Sons (1993).
23. Z. Q. Cheng, C. W. Lim, and S. Kitipornchai, "Three-dimensional asymptotic approach to inhomogeneous and laminated piezoelectric plates," *Int. J. Solids Struct.*, **37**, 3153–3175 (2000).

Received 23. 11. 2011